



Publication Year	2023
Acceptance in OA	2024-03-27T10:19:50Z
Title	The extremely high albedo of LTT 9779 b revealed by CHEOPS. An ultrahot Neptune with a highly metallic atmosphere
Authors	Hoyer, S., Jenkins, J. S., Parmentier, V., Deleuil, M., SCANDARIATO, GAETANO, Wilson, T. G., Díaz, M. R., Crossfield, I. J. M., Dragomir, D., Kataria, T., Lendl, M., Ramirez, R., Peña Rojas, P. A., Vinés, J. I.
Publisher's version (DOI)	10.1051/0004-6361/202346117
Handle	http://hdl.handle.net/20.500.12386/35035
Journal	ASTRONOMY & ASTROPHYSICS
Volume	675

The extremely high albedo of LTT 9779 b revealed by CHEOPS

An ultrahot Neptune with a highly metallic atmosphere[★]

S. Hoyer¹, J. S. Jenkins^{2,3}, V. Parmentier⁴, M. Deleuil¹, G. Scandariato⁵, T. G. Wilson⁶, M. R. Díaz⁷, I. J. M. Crossfield⁸, D. Dragomir⁹, T. Kataria¹⁰, M. Lendl¹¹, R. Ramirez^{2,12}, P. A. Peña Rojas², and J. I. Vinés¹²

¹ Aix Marseille Univ, CNRS, CNES, LAM, Marseille, France
e-mail: sergio.hoyer@lam.fr

² Instituto de Estudios Astrofísicos, Facultad de Ingeniería y Ciencias, Universidad Diego Portales, Av. Ejército 441, Santiago, Chile

³ Centro de Astrofísica y Tecnologías Afines (CATA), Casilla 36-D, Santiago, Chile

⁴ Université Côte d'Azur, Observatoire de la Côte d'Azur, CNRS, Laboratoire Lagrange, France

⁵ INAF, Osservatorio Astrofisico di Catania, Via S. Sofia 78, 95123 Catania, Italy

⁶ Centre for Exoplanet Science, SUPA School of Physics and Astronomy, University of St Andrews, North Haugh, St Andrews KY16 9SS, UK

⁷ Las Campanas Observatory, Carnegie Institution of Washington, Colina El Pino, Casilla 601 La Serena, Chile

⁸ Department of Physics and Astronomy, University of Kansas, Lawrence, KS, USA

⁹ Department of Physics and Astronomy, The University of New Mexico, Albuquerque, NM 87106, USA

¹⁰ Jet Propulsion Laboratory, California Institute of Technology, 4800 Oak Grove Drive, Pasadena, CA 91109, USA

¹¹ Observatoire Astronomique de l'Université de Genève, Chemin Pegasi 51, 1290 Versoix, Switzerland

¹² Departamento de Astronomía, Universidad de Chile, Camino el Observatorio 1515, Las Condes, Santiago, Chile

Received 10 February 2023 / Accepted 14 May 2023

ABSTRACT

Context. Optical secondary eclipse measurements of small planets can provide a wealth of information about the reflective properties of these worlds, but the measurements are particularly challenging to attain because of their relatively shallow depth. If such signals can be detected and modeled, however, they can provide planetary albedos, thermal characteristics, and information on absorbers in the upper atmosphere.

Aims. We aim to detect and characterize the optical secondary eclipse of the planet LTT 9779 b using the CHaracterising ExOPlanet Satellite (CHEOPS) to measure the planetary albedo and search for the signature of atmospheric condensates.

Methods. We observed ten secondary eclipses of the planet with CHEOPS. We carefully analyzed and detrended the light curves using three independent methods to perform the final astrophysical detrending and eclipse model fitting of the individual and combined light curves.

Results. Each of our analysis methods yielded statistically similar results, providing a robust detection of the eclipse of LTT 9779 b with a depth of 115 ± 24 ppm. This surprisingly large depth provides a geometric albedo for the planet of $0.80^{+0.10}_{-0.17}$, consistent with estimates of radiative-convective models. This value is similar to that of Venus in our own Solar System. When combining the eclipse from CHEOPS with the measurements from TESS and *Spitzer*, our global climate models indicate that LTT 9779 b likely has a super metal-rich atmosphere, with a lower limit of $400\times$ solar being found, and the presence of silicate clouds. The observations also reveal hints of optical eclipse depth variability, but these have yet to be confirmed.

Conclusions. The results found here in the optical when combined with those in the near-infrared provide the first steps toward understanding the atmospheric structure and physical processes of ultrahot Neptune worlds that inhabit the Neptune desert.

Key words. planets and satellites: fundamental parameters – planets and satellites: atmospheres – techniques: photometric – planets and satellites: individual: LTT9779b – planetary systems

1. Introduction

Occultation measurements of giant planets that pass directly behind their host star are a powerful tool that allows us to probe various aspects of planetary atmospheres in great detail. A global picture can be constructed that allows modeling the thermal properties, chemistry, and physical processes of the planet, particularly when using highly sensitive machinery to extract very weak emission signatures. The CHaracterising ExOPlanet

Satellite (CHEOPS; [Benz et al. 2021](#)) is one such space-based observatory that allows optical reflectance measurements of transiting planets to be made at very high photometric precision. For example, [Lendl et al. \(2020\)](#) were able to measure the secondary eclipse of the hot Jupiter WASP-189 b with a precision of only 4.3 ppm. The CHEOPS observations also revealed an asymmetric transit shape, indicating that gravity darkening due to the host star's rapid rotation is at play.

Other recent examples are the occultation measurements of the first known transiting planet, HD 209458 b (with an eclipse depth of 20 ± 3.3 ppm; [Brandeker et al. 2022](#)), and of the benchmark hot giant HD 189733 b (with an eclipse depth

[★] CHEOPS data are available in the ESA mission archive: https://cheops-archive.astro.unige.ch/archive_browser

of 24.7 ± 4.5 ppm; Krenn et al. 2023). These extremely precise eclipse measurements highlight that CHEOPS has the power to allow planetary atmospheric investigations to be performed at optical wavelengths.

The optical spectra of a planet are often a combination of thermal emission and reflected light. This complicates albedo measurements when only optical data are available. For planets hotter than ≈ 2000 K, the optical flux measured by the *Kepler* and Transiting Exoplanet Survey Satellite (TESS) spacecrafts is dominated by the thermal emission of the planet, rendering a measurement of the optical geometric albedo highly model dependent (Heng & Demory 2013; Parmentier et al. 2016; Gao et al. 2021). Thermal emission is a minor contributor to the optical flux for cooler planets. Esteves et al. (2015) showed that hot Jupiters generally have low geometric albedos of about 0.1, with the notable exceptions of Kepler-7 b ($A_g=0.35$; Demory et al. 2013) and Kepler-13 Ab (0.33; Shporer et al. 2014). The high albedo of Kepler-13 Ab was corroborated by Wong et al. (2021) using TESS data ($A_g=0.53 \pm 0.15$). In the same work, they also reported a geometric albedo of 0.45 ± 0.16 for the brown dwarf KELT-1b.

Similarly, smaller rocky planets also tend to exhibit low geometric albedos, whose values are generally consistent with zero (Sheets & Deming 2017), although there are notable examples with significantly higher values such as Kepler-10 b, which maintains a value of 0.58 ± 0.25 (Esteves et al. 2015). Results for hot Neptunes are rare because we lack a genuine sample to study.

The albedo of a planet can be understood as the competition between the scattering of light (either due to gaseous Rayleigh scattering or Mie scattering by clouds) and the absorption of the light by molecular species. The dayside of ultrahot Jupiters such as WASP-121 b is likely devoid of clouds and possess strong optical absorbers such as titanium and vanadium oxide, causing their albedo to be low (Parmentier et al. 2018; Bourrier et al. 2020). In planets cooler than 2000 K, sodium and potassium become the strongest optical absorbers, meaning that the albedo of cloudless planets tends to be extremely low (Sudarsky et al. 2000; Parmentier et al. 2015).

LTT 9779 b is the first detected ultrahot Neptune (Jenkins et al. 2020). With a 0.79 day orbital period and a size of $4.72 R_\oplus$, it was the first planet to populate the so-called Neptunian desert. With an equilibrium temperature of 1978 ± 19 K, LTT 9779 b sits at the boundary between planets with a near-infrared (NIR) flux dominated by thermal emission and an optical flux dominated by reflected light. The planet is an excellent benchmark because its secondary eclipse has been observed in the infrared by the *Spitzer* Space Telescope and in the optical with TESS. Using *Spitzer*, Dragomir et al. (2020) and Crossfield et al. (2020) were able to measure the NIR occultations and phase curve for the planet, revealing a strong thermal emission that is disrupted in the redder $4.5 \mu\text{m}$ bandpass by molecular absorption, likely that of CO. In addition, a dayside brightness temperature of ~ 2100 K was found, with a nightside cooler by about 1100 K. This means that the heat redistribution around the planet is weak. These results provide strong constraints on the thermal emission expected in the optical from the planet, allowing a much better idea of the true geometric albedo as soon as an optical eclipse can be measured. Interestingly, the TESS marginal optical measurement showed a planet that is brighter than would be expected when extrapolating the thermal emission of the planet, pointing toward the possibility of a high albedo (Dragomir et al. 2020). However, with only one data point in the optical, molecular emission features could not be ruled out, and the conclusion of a high geometric albedo could not be made.

In this work, we show the results from ten occultation events of LTT 9779 b observed by CHEOPS. The occultations provide a strong constraint on the geometric albedo of the planet and allow us to test for evidence of variability in the planetary atmosphere. In Sect. 2 we discuss the target star and its known properties. In Sect. 3, we then highlight the CHEOPS observations, and in Sect. 4 we show how the data were processed and analyzed to provide the final light curves and models. In Sect. 5, we compare the observational constraints with atmospheric modeling of the planet, and in Sect. 6, we finally summarize our main findings and place them in context with our current knowledge of the field.

2. Characteristics of LTT 9779

Together with the confirmation of the planetary nature of LTT 9779 b, Jenkins et al. (2020) also reported a precise characterization of the host star. In this work, we refer to the stellar properties reported there, but we summarize the main characteristics here.

LTT 9779 has a visual brightness of 9.76 mag. With a *Gaia* DR2 (Gaia Collaboration 2018) parallax of 12.403 ± 0.049 mas, it is located at a distance of 80.63 pc. High-resolution ground-based spectroscopy together with spectral energy distribution (SED) calculations with ARIADNE (Vines & Jenkins 2022) allowed the estimate that LTT 9779 is a G7V star and has an effective temperature of $T_{\text{eff}} = 5471 \pm 32$ K, a $\log g$ of 4.47 ± 0.11 dex, and an $[\text{Fe}/\text{H}]$ of $+0.25 \pm 0.05$ dex by employing the codes SPECIES (Soto & Jenkins 2018) and ZASPE (Brahm et al. 2017). Jenkins et al. (2020) also determined the stellar mass, radius, and age. They provided values of $1.02^{+0.02}_{-0.03} M_\odot$, $0.949 \pm 0.006 R_\odot$, and $2.0^{+1.3}_{-0.9}$ Gyr. Based on the bulk properties in general, LTT 9779 therefore is a main-sequence solar analog star.

Beyond the bulk parameters, the high-resolution spectra also allowed measuring the rotation velocity and activity status of the star. These are two key properties when considering the stability of the photometric data sets that are used to constrain the eclipse model. LTT 9779 was found to rotate very slowly, with a $v \sin i$ of only $1.06 \pm 0.37 \text{ km s}^{-1}$. This value is close to the integrated rotation velocity of the Sun (1.6 km s^{-1} ; Pavlenko et al. 2012). The star is also as inactive as the Sun, with a HARPS measured $\log R'_{\text{HK,HARPS}}$ value of -5.10 dex. These values agreed with the residual scatter in the TESS photometric light curve after fitting the transit model, proving that LTT 9779 is an excellent candidate for optical precision photometry. More details about the stellar characterization can be found in the methods section of Jenkins et al. (2020).

3. CHEOPS observations

We have gathered ten CHEOPS observations or visits of LTT 9779 during the predicted secondary eclipses of the hot Neptune planet. The visit durations were planned to be 5 h long (about three CHEOPS orbits) in order to encompass the full occultation and enough data before and after the event. In Table 1 we present the observation log of each visit. It is known that CHEOPS observations present interruptions during each orbit due to high levels of stray light (SL), Earth occultations, and/or South Atlantic Anomaly (SAA) crossings, periods for which the data are not downlinked to Earth (Benz et al. 2021). For the visits presented in this work, the interruptions were mostly produced by high levels of SL, and its effect on the efficiency of the visit is

Table 1. CHEOPS observation logs of LTT 9779.

Visit	Obs. start UTC date	Obs. end UTC date	Duration (h)	Exposure Time (s)	CHEOPS file key	Efficiency (%)	Eclipse Coverage (%)
1	2020-09-25T13:56:53	2020-09-25T18:41:01	4.73	60	CH_PR410001_TG000101	74.4	92
2	2020-09-26T08:38:07	2020-09-26T13:20:15	4.70	60	CH_PR410001_TG000102	69.2	77
3	2020-09-27T03:32:53	2020-09-27T08:17:01	4.73	60	CH_PR410001_TG000103	73.0	61
4	2020-09-27T22:59:27	2020-09-28T03:29:34	4.50	60	CH_PR410001_TG000104	81.5	92
5	2020-09-28T17:43:53	2020-09-28T23:17:02	5.55	60	CH_PR410001_TG000105	69.4	61
6	2020-10-01T02:48:47	2020-10-01T07:16:54	4.47	60	CH_PR410001_TG000106	78.0	96
7	2020-10-12T23:55:27	2020-10-13T04:21:34	4.44	60	CH_PR410001_TG000107	79.4	100
8	2020-10-16T22:47:53	2020-10-17T04:20:02	5.54	60	CH_PR410001_TG000108	68.1	54
9	2020-10-18T13:25:07	2020-10-18T17:41:14	4.23	60	CH_PR410001_TG000109	71.6	69
10	2020-10-26T11:05:52	2020-10-26T15:55:00	4.82	60	CH_PR410001_TG000110	58.6	83

reported in Table 1. In addition, we also report in the last column of Table 1 the time coverage of the observations during eclipse using the ephemeris and transit duration from [Dragomir et al. \(2020\)](#) and [Crossfield et al. \(2020\)](#). The raw data of each visit are automatically processed by the CHEOPS data reduction pipeline (DRPv13.1, [Hoyer et al. 2020](#)). The DRP delivers aperture photometry of the target extracted from the instrumental calibrated (i.e., bias, gain, linearization, and flat fielding) and corrected data (background, cosmic rays, and smear). Of the four photometric apertures used by this version of the DRP, we chose the light curves obtained with the DEFAULT aperture ($R=25$ pix) because it gives the best performance in terms of light-curve dispersion.

In the field of view (FoV) of LTT9779 lie two superposed close-by stars of $G = 19$ and $G = 15$ which distance from the target is $19''$ and $21''$, respectively, as shown in Fig. 1. The pixel scale of CHEOPS CCD is $1''$. The $G = 19$ source (labeled 1 in Fig. 1) is barely detected in CHEOPS science images, while the $G = 15$ star (labeled 2) is observed within the DEFAULT aperture (represented by the yellow circle). The well-known rotation of the satellite ([Benz et al. 2021](#); [Hoyer et al. 2020](#)) produces the apparent rotation of the background stars around the pointing direction through the observations. Due to the inhomogeneous and asymmetric shape of the CHEOPS point spread function (PSF), as shown in Fig. 1, the photometric contamination produced by background sources varies as a function of the roll angle of the satellite. The DRP estimates and delivers the contamination produced by background stars within the photometric apertures from ad hoc simulations created by the DRP based on *Gaia* catalog (DR2; [Gaia Collaboration 2018](#)). An example of a frame of these simulations is shown in the bottom panel of Fig. 1. In Fig. 2, we show the normalized light curve of visit 2 (top panel) and its respective contamination curve (bottom panel). The chosen DEFAULT aperture minimizes the effect of the contamination without compromising the flux level of the target star.

4. Analysis and results

Contamination estimates of a single visit can suffer from artificial variations that are related to small changes (0.5 – 1 pix) in the relative distance between the target and contaminants due to rounding effects of intra-pixel distances in the simulations. To minimize this effect and to take advantage of the information available from all the visits, we combined the contamination light curves of the ten visits as a function of the roll angle. With this, we created a master contamination curve given by

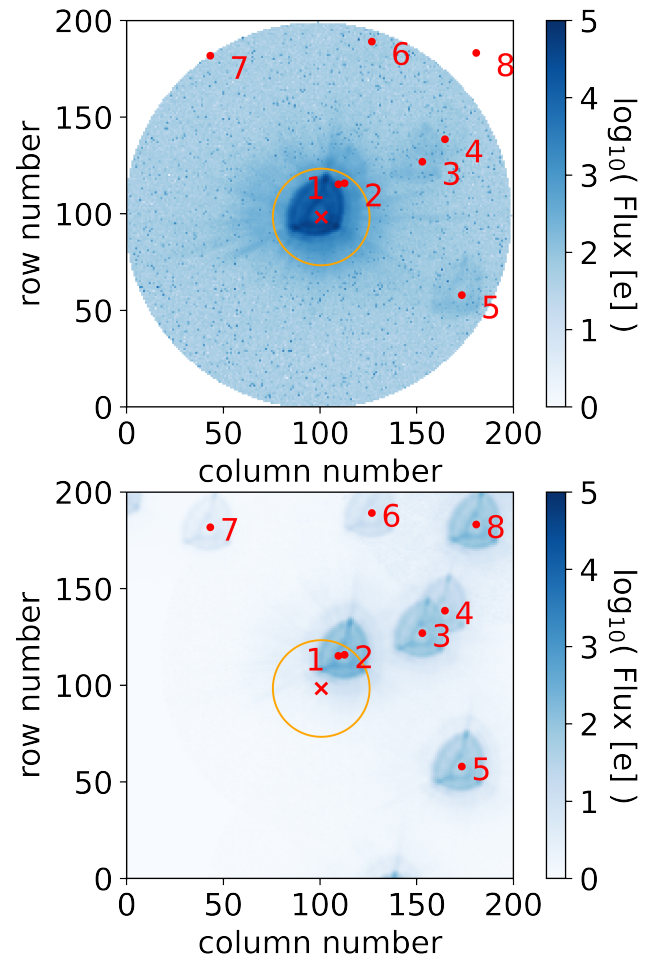


Fig. 1. Field of view of LTT 9779. The FoV observed by CHEOPS ($200 \times 200''$) is shown in the top panel, while the DRP-simulated field without the target is shown in the bottom panel. The red numbers and points mark the location of background stars.

the rolling mean of the combined curve. We interpolated this master contamination curve to calculate the contamination at the respective roll angle values of the images/points of each visit. An example of this contamination curve for visit 2 is shown in the bottom panel of Fig. 2. Finally, these new smooth contamination curves were used for the correction of the individual light curves, as described below.

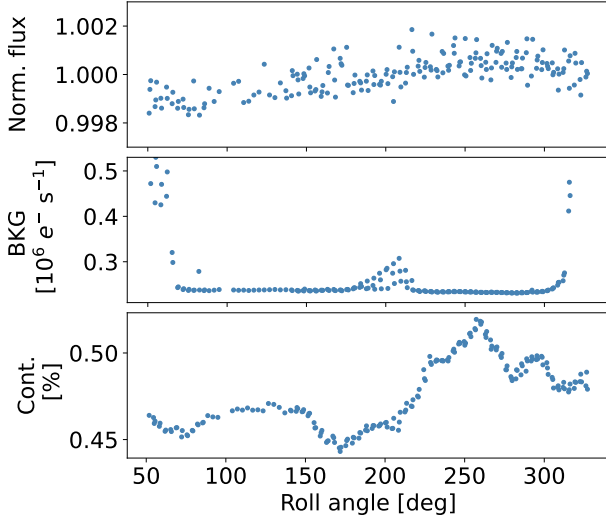


Fig. 2. Example of the flux, background, and contamination curves of LTT 9779. The top panel shows the raw normalized flux (DEFAULT aperture) of CHEOPS visit 2 as a function of the roll angle. The corresponding curves of the background and contamination produced by nearby stars are shown in the middle and bottom panels, respectively.

4.1. Light-curve trends

As a first step, we studied the datasets individually in order to perform a detailed analysis of each light curve that gave us the best possible photometric quality of each observation. Thus, we removed large outlier points that are generally produced by high levels of background flux and/or cosmic-ray hits. We also observed variations in the light curve that were produced, as mentioned above, by the contamination of background sources inside and nearby the photometric aperture. We also noted a second-order effect on the quality of the photometry. We identified, for example, small variations in the background levels (outside the regions of very high SL) whose origin we were unable to identify. It is known that bright sources (e.g., the Moon or very bright stars) close to the CHEOPS pointing direction can produce internal reflections in the satellite (e.g., Bonfanti et al. 2021) that contaminate the background region and/or the photometric aperture, usually as a function of the roll angle. In this case, we were unable to identify a particular source of this background variation. In the middle panel of Fig. 2, we show an example of these background variations around the roll angle $\sim 200^\circ$ in visit 2. In some visits, the effect was easily identifiable (in the form of a spike in the light curve at a specific roll angle range), but in others, it was more diffused or undetected.

4.2. Modeling of the occultations

We used the PYCHEOPS package (v1.0.14; Maxted et al. 2022) to modeling and detrend the occultation light curves. It includes, among other packages, LMFIT (Newville et al. 2020) for the nonlinear least-square minimization, EMCEE (Foreman-Mackey et al. 2013) for the Bayesian analysis, and the qpwr2 algorithm (Maxted & Gill 2019) to generate the transit or eclipse models.

PYCHEOPS allows using several detrending parameters while simultaneously fitting the eclipse model (see a detailed description in Maxted et al. 2022). To do this, it can use complementary information provided by the DRP (e.g., background, contamination flux of nearby stars, target centroids, and smear contamination) or directly the flux as a function of time or roll angle. In

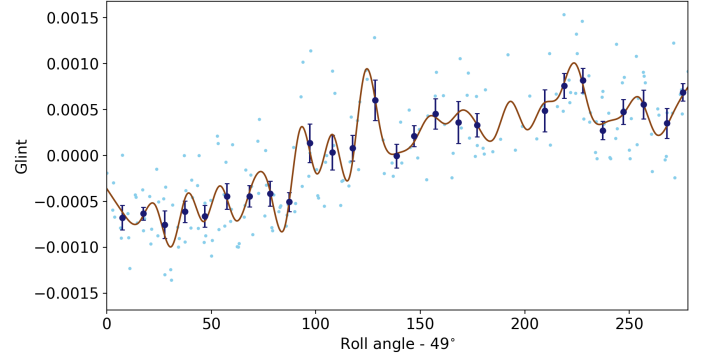


Fig. 3. Glint function fit for visit 1. The photometric points (light blue symbols) and its 10° bins (dark blue symbols) are shown as a function of the roll angle. The fitted glint function consisting of splines with 35 knots is represented by the brown curve. The x-axis represents the roll angle minus an offset to account for gaps in the light curve to improve visualization.

a first approach, we tried to identify the relevant parameters for the detrending of each individual light curve. As a result of the strong degeneracy among the detrending parameters and because of the variable effects we described above, we finally opted to use the PYCHEOPS *glint* function. This method allows the use of splines to fit for glints or light-curve trends as a function of the roll angle. The number of spline knots (order of the *glint* function) is defined by the user. In our case, the number was between 20–35. The final chosen order was the best compromise between reducing the dispersion of the residuals and overfitting of the data based on the final RMS of the residuals and the Bayesian information criteria (BIC) of the occultation fit. In Fig. 3 we show an example of the fitted *glint* function to the light curve of visit 1.

To model the individual light curves, we used the values of the orbital period (P) and transit reference time (T_0) from Crossfield et al. (2020) as priors for the fitted parameters. Each transit time (PYCHEOPS uses the mid-transit time instead of the mid-eclipse time) was estimated using this P and T_0 and propagating the uncertainties. The transit depth (D), transit width (W), and the impact parameter (b) were derived from the values reported in Jenkins et al. (2020), of which D and b were fixed in the fit. We assumed a circular orbit ($e = 0$) of the planet, which meant that the parameterization variables used by PYCHEOPS were set to zero ($f_c = e \cos \omega = 0$ and $f_s = e \sin \omega = 0$). As the focus of this study was on the detection of the occultations, we let the eclipse depth (L) free while the priors of the other parameters were constrained by normal distributions, whose width was defined by their respective reported uncertainties. As discussed above, we also included a flux-scaling factor (c) to model the out-of-eclipse flux, and the *glint* scale factor (g_s), which is a constant that scales the fitted *glint* model. A temporal variation of the flux was evident in the raw light curve of visit 10. We therefore also included a temporal linear function of the flux ($dfdt$) in the fit. We used noninformative priors for these two factors. Finally, PYCHEOPS also fits for the Gaussian white-noise term (σ_w), which we let be completely free. The priors used during the fitting are listed in Table 2. To sample the posterior probability distribution (PPD) of the model parameters, we used the Markov chain Monte Carlo (MCMC) method implemented in emcee with 256 walkers and 512 sampling steps after a burn-in phase of 512 steps. This secured the convergence of the fit.

The resulting values of the individual fits are reported in Table 3. In Fig. 4, we show the detrended light curves with the

Table 2. Priors of the fitted parameters.

Parameter		Units	Distribution
Transit depth	D	ppm	2070.3 (fixed)
Impact parameter	b	R_\star	0.9123036 (fixed)
Orbital period	P	d	$\mathcal{N}(0.79207022(69))$
Transit ref. time	$T_0 - 2450000$	BJD	$\mathcal{N}(8783.51636(27))$
Transit width	W	Phase	$\mathcal{N}(0.0419(58))$
Eclipse depth	L	ppm	$\mathcal{U}(1, 10^5)$
Flux scale factor	c	–	$\mathcal{U}(0, 2)$
Glint scale factor	g_s	–	$\mathcal{U}(0, 2)$
Flux vs time	$d\text{fdt}$	–	$\mathcal{U}(0, 1)$
Transit time ^(a)	$T_{c,i}(n)$	BJD	$\mathcal{N}(T_0 + n \times P)$

Notes. We used normal, $\mathcal{N}(\mu_0, \sigma_0)$, or uniform, $\mathcal{U}(\text{lower_limit}, \text{upper_limit})$, distributions for the priors of the fitted parameters. ^(a)The transit time for each visit was computed using P and T_0 reported here and projecting their respective uncertainties.

Table 3. Results of the fits of each CHEOPS light curve.

Visit #	Eclipse depth ^(a) (ppm)	Residuals RMS (ppm)	Eff. ^(b) (%)	Detrending parameters ^(c)
1	253 ± 70	347	90	c, g_s
2	122 ± 81	447	75	c, g_s
3	149 ± 75	302	59	c, g_s
4	133 ± 54	263	86	c, g_s
5	109 ± 76	360	56	c, g_s
6	53 ± 41	266	96	c, g_s
7	51 ± 45	389	100	c, g_s
8	97 ± 63	313	54	c, g_s
9	54 ± 45	344	69	c, g_s
10	173 ± 66	324	84	$c, g_s, d\text{fdt}$

Notes. ^(a)The reported values correspond to the median and its 68% interval. ^(b)Efficiency of the observations during the eclipse. ^(c) c : flux scale factor. g_s : glint scale factor. $d\text{fdt}$: flux over time.

best eclipse model overplotted, while the raw light curves with the full model (detrending and eclipse) are shown in Figs. A.1 and A.2. As reported in Table 1 and visible in Fig. 4, the efficiency (coverage) of the eclipse during each observation ranged between 54 and 100%. In general, the interruptions of the observations were produced by the increase in the background level beyond the admitted CHEOPS observation limits. Thus, before and after these gaps, it is possible to find an increase in the photometric dispersion as well as in the number of outliers. Even after the filtering of the points with high background levels, it is possible to see that the photometric points before/after the gaps show a larger dispersion and/or trends when compared to the rest of the light curve. In order to confirm that the fitted values of the eclipse depths were not driven by these points, we performed a more aggressive filtering of the light curves. This filtering usually consisted of removing a significant number of photometric points at the ends of the CHEOPS orbits and/or of removing outliers after a high-order polynomial fit of the flux versus time or roll angle. The fitted values of the occultation depths obtained by fitting these light curves are fully consistent, well within 1σ with the previous results (method 2 in Fig. B.1).

We also confirmed our results with a fully independent approach regarding the filtering, detrending, and modeling of

the light curves as described below. The full description of this approach is described in detail in Scandariato et al. (2022). In summary, for each visit, we fixed the ephemeris of the system to the ephemerides reported by Crossfield et al. (2020) and fit the decontaminated light curves extracted by the DRP with a model that simultaneously included the instrumental correlated noise and the occultation signal. The instrumental correlated noise is the superposition of a linear trend in time plus a periodic function of the telescope roll angle, the latter being the harmonic expansion up to the second harmonic of the orbital frequency of CHEOPS. We explored the parameter space in a Bayesian framework by maximizing the likelihood of the model using the EMCEE Python package. We used physically meaningful uninformative priors and let 30 walkers run for 50,000 steps to ensure convergence. The results of this approach are fully consistent with those obtained with *pycheops*. The results of the fitted eclipse depths by the three methods are shown in Fig. B.1.

4.3. Multivisit modeling

We describe the results of the simultaneous fitting of all the light curves below. At the end of the section, we compare these results with the values obtained by fitting only the visits with clear eclipse detections in the previous section.

In a first step, in order to enhance the significance of the occultation detection, we simultaneously fit the 10 CHEOPS visits using the *Multivisit* method available in *pycheops*. For this fit, we used the same priors as for the individual modeling. We also fit for the normalization factor (c) and the glint scale (g_s) of each light curve, and we fit for a single value of the eclipse depth (L) with all the light curves simultaneously. In this case, for the MCMC fit, we used 1024 burning and sampling steps while adopting 512 walkers. The resulting best model is shown in Fig. 6 (top panel) plotted over the combined phased light eclipse curve. The corner plot with the posteriors of all the fitted parameters is shown in Fig. C.1. The eclipse depth obtained from the simultaneous fit of the ten visits is $L = 115 \pm 24$ ppm, which is unexpectedly high when compared to the value obtained from TESS (59^{+24}_{-21} ppm, Dragomir et al. 2020).

The estimates of the eclipse depth obtained by fitting the CHEOPS light curves individually (Sect. 4.2) are consistent within 1σ with the value retrieved from the multivisit analysis described above (except for the value of visit 1; see Fig. 5). We note, however, that some eclipses tend to be larger than 100 ppm (numbers 1, 2, 3, 4, 5, and 10), while the eclipse is more shallow in the remaining light curves. We found no correlation between the estimated individual eclipse depths and the efficiency of the observations during the eclipse and/or the quality of the observation (using the RMS of the residuals as a proxy), as reported in Tables 1 and 3. Thus, to explore a potential variability effect in the eclipses, we performed a simultaneous multivisit fit for the light curves with only high or lower eclipse values. We obtained an eclipse depth of $L = 163 \pm 32$ ppm and $L = 50 \pm 32$, respectively, and their combined light curves are shown in Fig. D.1. Although these fits show two distinct values (see Fig. D.2), we cannot statistically confirm a variability effect with the data we used because the individual detections have a low significance.

5. Atmospheric modeling

5.1. Model description

In order to model the atmosphere of LTT 9779 b, we used the radiative-convective equilibrium model *ScCHIMERA* (see

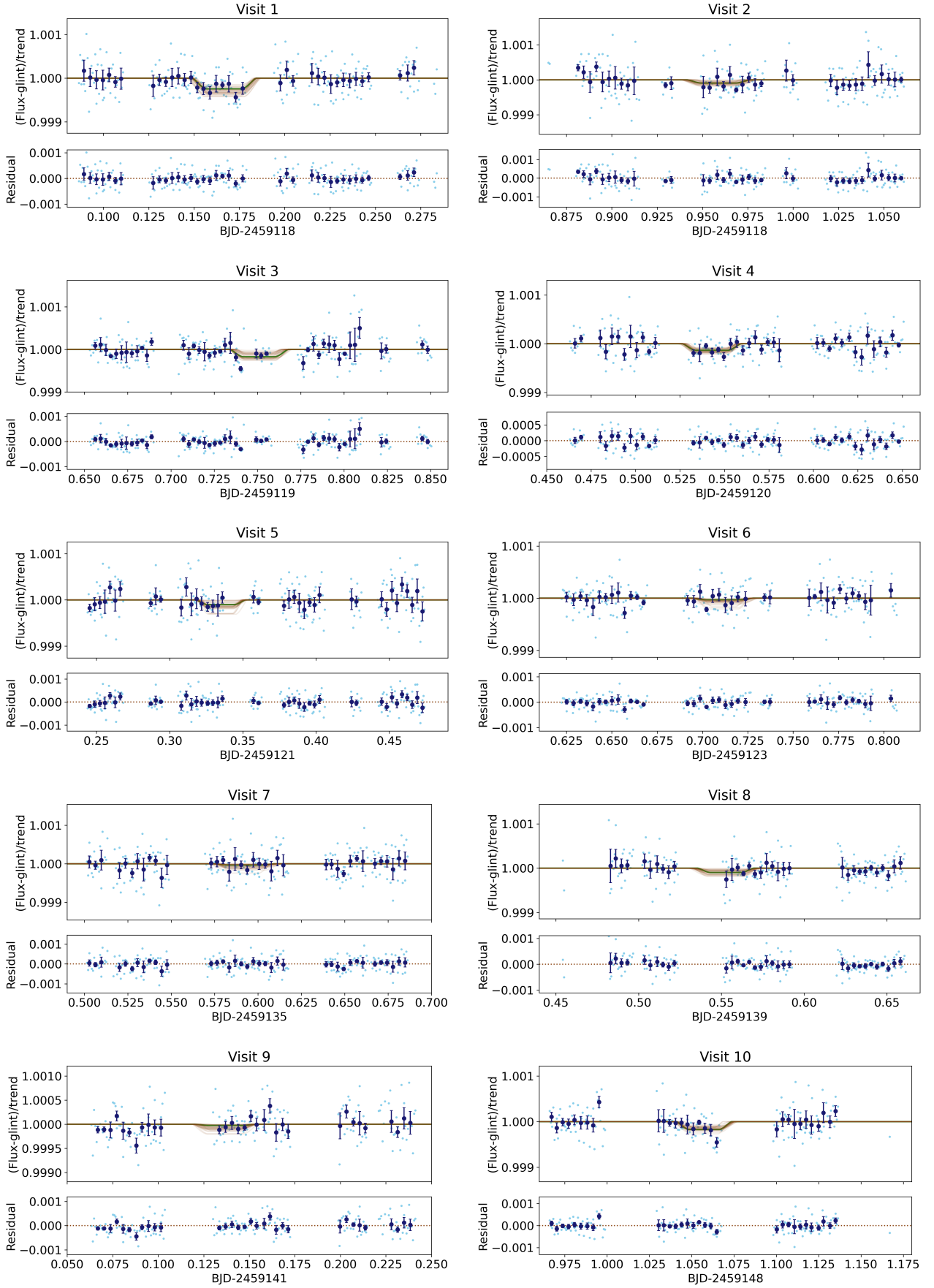


Fig. 4. Detrended CHEOPS light curves of the ten eclipses of LTT 9779 b. The corrected light curves and their 5 min bins are shown with the light and dark blue symbols, respectively. The sample of 32 fitted eclipse models is represented with the brown curves. The residuals are shown in the bottom panel of each light curve.

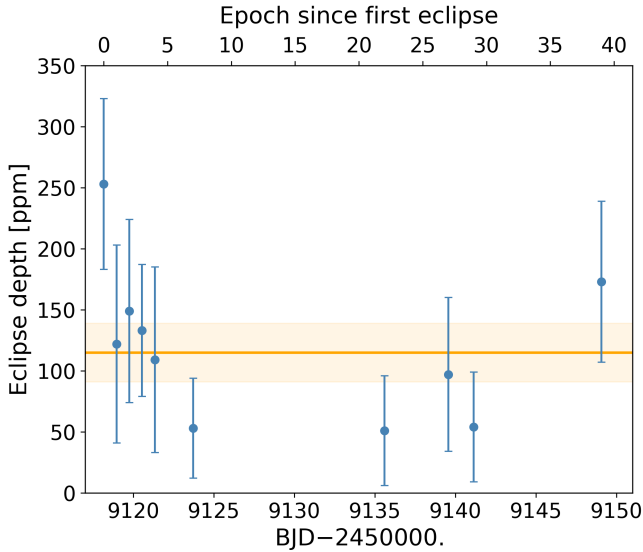


Fig. 5. Eclipse depths obtained by fitting the CHEOPS light curves of LTT 9779 b individually. The orange curve and shaded region represent the estimated eclipse depth and its 1σ intervals obtained by fitting the 10 visits simultaneously.

Arcangeli et al. 2018; Piskorz et al. 2018; Mansfield et al. 2021, for details). The model assumes thermochemical equilibrium, where elemental abundances of metals are enriched by a given factor, called metallicity, compared to the solar composition values of Lodders et al. (2009). The model further assumes that part of the stellar irradiation is transferred to the planet nightside and that the dayside radiative-convective equilibrium is equivalent to the equilibrium where the total received flux is fT_{eq}^4 . Here, f is the redistribution factor, which ranges from 1 for a full redistribution to 2 for a dayside-only redistribution. It is 2.66 for no redistribution.

We wished to determine whether scenarios under the radiative-convective equilibrium assumption can reasonably match both the optical (CHEOPS and TESS) and the infrared (*Spitzer*) data. In particular, we aimed to find a model that can produce a high brightness temperature in the optical while keeping a low brightness temperature in the infrared. Clouds would increase the optical data significantly while keeping the atmosphere cold enough to match the infrared observations. As a consequence, we used the model to determine the conditions that are needed to reflect clouds so that they form on the dayside of this planet.

The temperature of LTT 9779 b is high. In order to study the extreme cases, we decided to consider titanium-based condensates, which are the most refractory condensates that can form in hot exoplanets together with silicate clouds, which have often been considered in previous studies of hot Jupiters (Lecavelier des Etangs et al. 2003; Parmentier et al. 2016; Wakeford et al. 2017). Whereas silicate clouds have been used in previous studies with the ScCHIMERA code (Mai & Line 2019), we had to specifically include titanium-based condensates inside the code. Because the equilibrium condensation chemistry of titanium is complex, we decided to consider all the species as a single “titanium cloud” that are predicted to condense by the chemical equilibrium applications (CEA) code: Ti_4O_7 , MgTi_2O_5 , Ti_3O_5 , Ti_4O_7 , CaTiO_3 , Ti_4O_7 , $\text{Ca}_4\text{Ti}_3\text{O}_{10}$, $\text{Ca}_3\text{Ti}_2\text{O}_7$, and Ti_2O_3 . We then considered this titanium cloud to have the same optical properties as CaTiO_3 clouds. We further used the (Ackerman & Marley 2001) framework to determine the vertical extent of

the clouds. The model has two parameters: the sedimentation efficiency, which determines the vertical extent of the cloud, and the vertical mixing rate, which determines the particle sizes (see, e.g., Christie et al. 2021). For this first exploration, we fixed both parameters, $K_{zz} = 10^5 \text{ m}^2 \text{ s}^{-1}$ and $f_{\text{sed}} = 0.1$. This high value of K_{zz} is roughly in line with estimates for hot-Jupiter atmospheres (Parmentier et al. 2013; Komacek et al. 2019), whereas the low value of f_{sed} was chosen specifically to favor small highly reflective cloud particles (Ackerman & Marley 2001; Gao et al. 2018).

5.2. Models with full redistribution

In order to find the minimum conditions for forming highly reflecting clouds in LTT 9779 b, we first computed a series of models assuming that heat is efficiently transported from the dayside to the nightside of the planet. This provided us with the coolest models that can be achieved under the assumption of radiative-convective equilibrium.

Figure 7 shows the spectra and the thermal profile of four ScCHIMERA models assuming full redistribution and metallicities ranging from solar to 1000 times solar. Although they are unrealistic for such a hot planet, full redistribution models lead to the coolest possible thermal profiles and are thus a lower limit for cloud formation. If the thermal profiles of the full redistribution cases are too hot to form clouds, then no model with this set of parameters provides a high albedo.

The optical spectrum of Fig. 7 shows that all models except for the cases with 400 and 1000 times solar metallicity predict fluxes in the optical that are too low compared to the CHEOPS and TESS observations, but they produce thermal emission that is too high compared to the *Spitzer* 4.5 μm band. In contrast, the models with 400 and 1000 times solar metallicity predict a much higher optical flux and a lower infrared flux. This marks the appearance of silicate clouds. They increase the geometric albedo from <0.01 to 0.45 in the CHEOPS bandpass and the Bond albedo from <0.01 to 0.75.

Clouds are naturally easier to form in higher metallicity atmospheres because more material is available. Cloud formation relies on the partial pressure of material. For a given atmospheric pressure, the partial pressure of condensing species increases with metallicity, and clouds can form at hotter temperatures. This is highlighted in the bottom panel of Fig. 7. The figure shows that the condensation curves for the silicate and titanium clouds are strongly dependent on metallicity. As a consequence, we predict that only atmospheres with a metallicity higher than 400 times solar possess condensation temperatures that are high enough for both titanium and silicate clouds to condense and to form a thick reflective cover that increases the albedo of the planet.

The presence of silicate clouds can be inferred from the spectra in all models with metallicities higher than 400 times solar by specifically considering the weak silicate absorption feature around 8–12 μm . We used the tool PandExo (Batalha et al. 2017) to estimate that the observation of five LTT 9779 b eclipses with JWST/MIRI would lead to a detection of this silicate feature at 10 microns.

The comparison of the titanium-bearing molecule condensation curve (dotted line) and the thermal profiles of the models (solid lines) in the bottom panel of Fig. 7 shows all the models are cold enough for titanium-bearing molecules to condense. As a consequence, none of the models shows a thermal inversion due to the absorption of light by gaseous titanium oxide. However, the titanium oxide clouds never reach an optical depth that

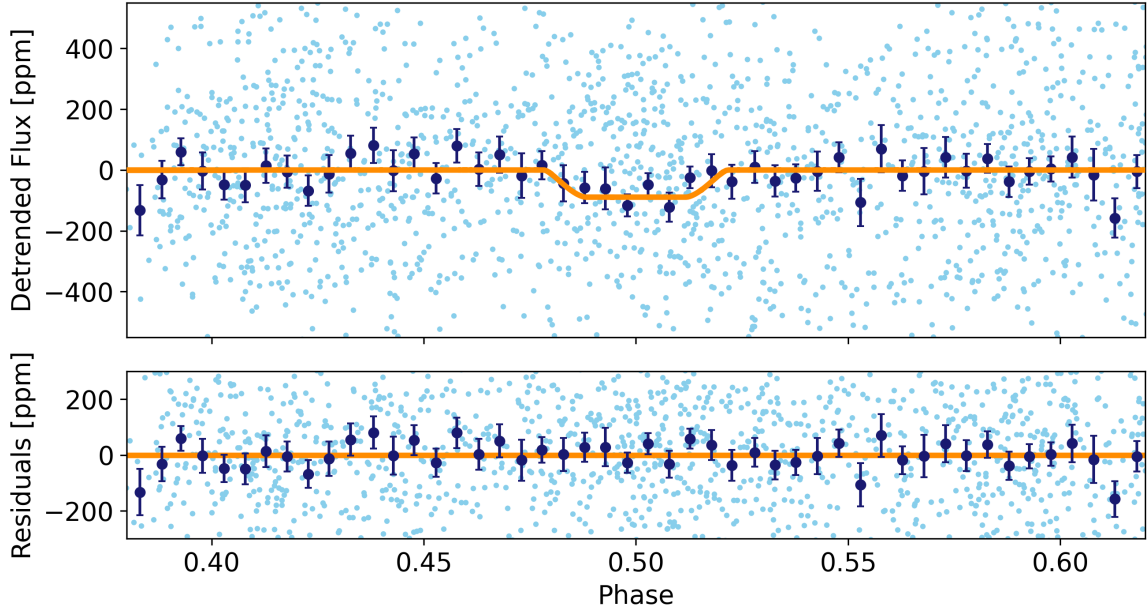


Fig. 6. Simultaneous fit of the CHEOPS light curves during the eclipses of LTT 9779 b. The combined phased light curve of the 10 CHEOPS visits and its 7 min bins are shown with the light and dark blue symbols, respectively. The best-fit model is represented by the yellow curve, and the residuals to this model are shown in the bottom panel.

is high enough to produce a high albedo. Only the condensation of silicate-based clouds can produce a high albedo and thus a large eclipse depth in the optical.

We conclude that a high albedo and thus the presence of clouds is necessary to explain both the infrared and optical observations of LTT 9779 b. In order for optically thick clouds to form, our models suggest that the planetary metallicity must be higher than 400 times solar. In planets that are more metal poor, the temperature for the condensation point of silicate clouds is too low, and no silicate clouds can form.

5.3. Models with varying heat redistribution

Heat redistribution from day to night is often poorly efficient. It was shown by theoretical models that hot planets should become less efficient at transporting heat from day to night than cold planets because hot gas can cool much faster radiatively than cold gas (Komacek et al. 2017; Parmentier & Crossfield 2017; Parmentier et al. 2021). Based on previous work on hot Jupiters, LTT 9779 b with its brightness temperature in the infrared close to 2000 K is expected to have a heat redistribution factor higher than 1 and possibly up to 2 (Parmentier et al. 2021). A higher heat redistribution factor will increase the dayside temperature of the planet.

In Fig. 8, we highlight the role of the redistribution in changing the spectra of the planet by fixing the metallicity to 1000 times solar and varying the redistribution factor (f) from 1 (full redistribution) to 2.6 (no redistribution). Even though clouds do form in the model without any heat redistribution, TiO and VO are able to evaporate again at low pressure, ensuring a strong thermal inversion. The geometric albedo of the planet in the CHEOPS bandpass is then 0.53, and the Bond albedo is 0.43. The eclipse depth in the optical is due equally to reflected light and to the emission inside TiO and VO bands. Overall, this no-redistribution case is too hot to match the infrared points.

For lower values of the heat redistribution factor, TiO/VO condenses out of the atmosphere and the planetary albedo increases. The geometric albedo (A_g) in the CHEOPS bandpass

reaches 0.75 for the $f = 1.75$ case and 0.66 for the $f = 1.5$ case. The combined effect of the Bond albedo (reaching $A_B = 0.7$ in both cases) and the heat redistribution makes the dayside much cooler and the thermal emission much lower. Models with an intermediate heat redistribution factor (1.75 and 1.5) can provide a reasonable match to both optical and infrared data. Models with full redistribution ($A_g = 0.45$ and $A_B = 0.76$) are too cold to match the infrared data. We note that none of the models can match both *Spitzer* points, but they provide a reasonable match to their average flux.

6. Discussion and conclusions

The contribution of the reflected light of LTT 9779 b and of the thermal component (assuming blackbody emission) in the CHEOPS bandpass, assuming different values of geometric albedos, is shown in Fig. 9. For LTT 9779 b, the thermal component starts to become significant at temperatures above 2500 K, which are even hotter than the dayside temperatures measured in the *Spitzer* bands (Dragomir et al. 2020; Crossfield et al. 2020). In particular, we estimate $A_g = 0.8^{+0.10}_{-0.17}$ assuming there is no thermal contribution in the CHEOPS bandpass. Thus, only $A_g > 2/3$ is consistent with our measured occultation depth, which in the Lambertian approximation also indicates a very high Bond albedo. This is also consistent with the estimate of $A_B \approx 0.7$ of Crossfield et al. (2020) based on the $4.5 \mu\text{m}$ *Spitzer* data and with our findings from the radiative-convective model: models that matched the data best had geometric albedos up to 0.75.

This means that LTT 9779 b is the exoplanet with the highest measured albedo, comparable to that of Venus. It stands out among the gaseous planets with albedos measured in the optical (see, e.g., Fig. 4 of Krenn et al. 2023). Before, only Kepler-1658 b was reported to have a similarly high albedo $A_g = 0.724 \pm 0.090$ (Chontos et al. 2019), but this estimate does not properly account for the thermal component contribution from thermal emission and/or tidal dissipation, as discussed in Vissapragada et al. (2022) for this planet or in Lendl et al. (2020) for the case of WASP-189 b.

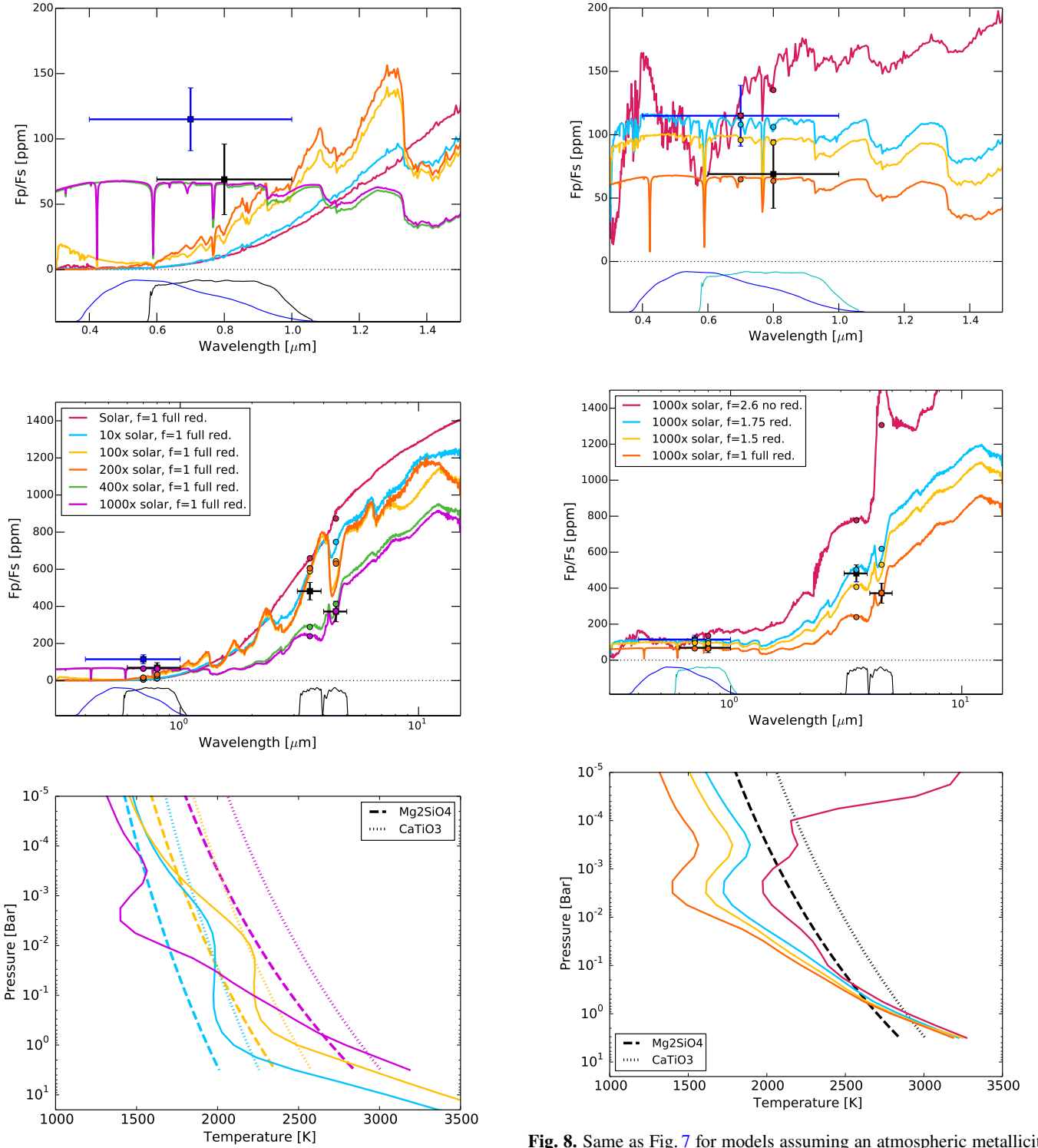


Fig. 7. Modeled optical (top) and optical+NIR (middle) spectrum of LTT 9779 b compared to the CHEOPS (blue symbol), TESS, and *Spitzer* (black symbols) observations for models assuming a full redistribution of heat and different metallicities. The respective scaled transmission curve of each instrument is also shown at the bottom of the panel. In the bottom panel, we show the modeled thermal profiles for a subsample of models together with the condensation curves of Mg_2SiO_4 and CaTiO_3 for different metallicities (color). The condensation curves scale with metallicity. The geometric albedos in the CHEOPS bandpass and Bond albedos are lower than 0.01 for metallicities lower than 200 times solar and increase to 0.45 and 0.75, respectively, for metallicities 400 times solar and higher.

Fig. 8. Same as Fig. 7 for models assuming an atmospheric metallicity of 1000 times solar and different redistributions of heat between the day- and nightside of the planet, ranging from no redistribution ($f = 2.66$) to full redistribution ($f = 1$). In the bottom panel, we show the modeled thermal profiles together with the condensation curves of Mg_2SiO_4 and CaTiO_3 . Geometric albedos in the CHEOPS bandpass are 0.53, 0.75, 0.66, and 0.45, and the Bond albedos are 0.43, 0.68, 0.72, and 0.75 for $f = 2.6, 1.75, 1.5$, and 1.

Our measured high albedo requires clouds that can survive the high stellar irradiation in the planetary dayside. Thus, our modeling of the LTT 9779 b atmosphere suggests a supersolar metallicity (at least higher than 400 times the solar abundance).

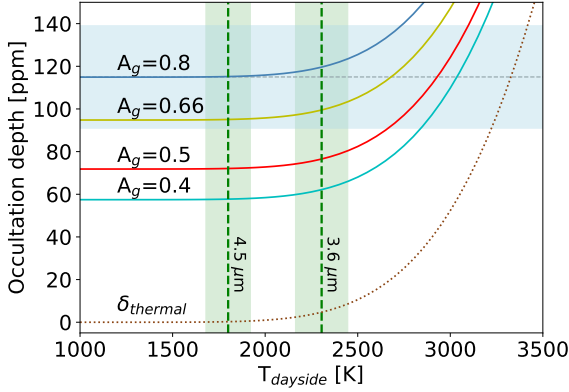


Fig. 9. Contribution of the reflected and thermal components in the occultation depth of LTT 9779 b for the CHEOPS wavelengths. The blue region marks the occultation depth ($\pm 1\sigma$) measured with CHEOPS. The dotted curve represents the thermal component, and the solid curves represent the summed contribution of the two components, i.e., including the effect of the reflected light for different geometric albedos (A_g). The vertical green bands show the dayside temperature measured with *Spitzer* at 3.6 and 4.5 μm .

Crossfield et al. (2020) also invoked a metal-rich atmosphere to explain the optical and infrared phase curves of LTT 9779 b. They suggested a supersolar metallicity when compared with their atmospheric models even without considering atmospheric condensates, as was the case for the analysis performed in this work.

In parallel, scenarios with an intermediate efficiency of heat redistribution between the day- and nightsides allow reconciling the optical measurements with the 3.6 and 4.5 μm *Spitzer* eclipses because a low redistribution would produce daysides at NIR bandpasses that are too hot (Fig. 8). If confirmed, the metal-rich atmosphere of this ultrahot planet can shed light on its evolution and current location in the middle of the so-called Neptunian desert (Mazeh et al. 2016). Atmospheric metallicity could have been enhanced by the effects of a strong extreme-UV photoevaporation, quickly removing the light volatiles from the upper layers of the already metal-rich early atmosphere (the stellar host has $\text{Fe}/\text{H} = +0.25$ dex; Jenkins et al. 2020). Alternatively, the planet might have been strongly evaporating, and when it reached an atmospheric metal enrichment high enough for clouds to form, the albedo of these clouds cooled the planet, which in turn suppressed the atmospheric escape. Finally, the upper atmosphere could have been ripped out by the tidal interaction with the stellar host (Roche-lobe overflow) during its formation, exposing the deeper layers of the planetary atmosphere. Massive planets at short orbital periods, such as LTT 9779 b, are expected to rapidly spiral-in and be destroyed at the stellar surface (e.g., Ginzburg & Sari 2017), however. This is compatible with the estimate of the spiral-in time of LTT 9779 b of 0.61 Gyr assuming a tidal quality factor of $Q_\star = 10^6$ – 10^7 in Eq. (6) of Collier Cameron & Jardine (2018) and the stellar host age ($2.1^{+2.2}_{-1.4}$ Gyr).

Additionally, we explored the possible variability of the eclipse depths of LTT 9779 b. The measured variation through CHEOPS observations is not significant because the signal-to-noise ratio of each of the individual eclipses is low. However, if it is real, the variability of the eclipses would imply a dynamic atmosphere, which would add a relevant component to the description of the atmosphere of this planet. The atmospheric variability can be further tested with more CHEOPS observations with a high signal-to-noise ratio, or with JWST observations in the NIR.

Acknowledgements. The authors acknowledge Mike Line for guidance using the scCHIMERA code. The contribution of LAM was supported by CNES, focused on CHEOPS, and S.H. acknowledges CNES funding through the grant 837319. This research has made use of computing facilities operated by CeSAM data center at LAM, Marseille, France. We also thank J.C. Meunier and J.C. Lamber for the support provided in the use of these facilities. J.S.J. acknowledges support by FONDECYT grant 1201371, and partial support from CONICYT project Basal AFB-170002. G.Sc. acknowledges support from CHEOPS ASI-INAF agreement no. 2019-29-HH.0. T.G.W. acknowledges support from STFC consolidated grant number ST/V000861/1. The contribution of M.L. has been carried out within the framework of the NCCR PlanetS supported by the Swiss National Science Foundation under grants 51NF40_182901 and 51NF40_205606. M.L. further acknowledges support of the Swiss National Science Foundation under grant number PCEFP2_194576. J.I.V. acknowledges support of CONICYT-PFCHA/Doctorado Nacional-21191829.

References

- Ackerman, A. S., & Marley, M. S. 2001, *ApJ*, **556**, 872
 Arcangeli, J., Désert, J.-M., Line, M. R., et al. 2018, *ApJ*, **855**, L30
 Batalha, N. E., Mandell, A., Pontoppidan, K., et al. 2017, *PASP*, **129**, 064501
 Benz, W., Broeg, C., Fortier, A., et al. 2021, *Exp. Astron.*, **51**, 109
 Bonfanti, A., Delrez, L., Hooton, M. J., et al. 2021, *A&A*, **646**, A157
 Bourrier, V., Kitzmann, D., Kuntzer, T., et al. 2020, *A&A*, **637**, A36
 Brahm, R., Jordán, A., Hartman, J., & Bakos, G. 2017, *MNRAS*, **467**, 971
 Brandeker, A., Heng, K., Lendl, M., et al. 2022, *A&A*, **659**, A4
 Chontos, A., Huber, D., Latham, D. W., et al. 2019, *AJ*, **157**, 192
 Christie, D. A., Mayne, N. J., Lines, S., et al. 2021, *MNRAS*, **506**, 4500
 Collier Cameron, A., & Jardine, M. 2018, *MNRAS*, **476**, 2542
 Crossfield, I. J. M., Dragomir, D., Cowan, N. B., et al. 2020, *ApJ*, **903**, L7
 Demory, B.-O., de Wit, J., Lewis, N., et al. 2013, *ApJ*, **776**, L25
 Dragomir, D., Crossfield, I. J. M., Benneke, B., et al. 2020, *ApJ*, **903**, L6
 Esteves, L. J., De Mooij, E. J. W., & Jayawardhana, R. 2015, *ApJ*, **804**, 150
 Foreman-Mackey, D., Hogg, D. W., Lang, D., & Goodman, J. 2013, *PASP*, **125**, 306
 Gaia Collaboration (Brown, A. G. A., et al.) 2018, *A&A*, **616**, A1
 Gao, P., Marley, M. S., & Ackerman, A. S. 2018, *ApJ*, **855**, 86
 Gao, P., Wakeford, H. R., Moran, S. E., & Parmentier, V. 2021, *J. Geophys. Res.: Planets*, **126**
 Ginzburg, S., & Sari, R. 2017, *MNRAS*, **469**, 278
 Heng, K., & Demory, B.-O. 2013, *ApJ*, **777**, 100
 Hoyer, S., Guterman, P., Demangeon, O., et al. 2020, *A&A*, **635**, A24
 Jenkins, J. S., Díaz, M. R., Kurtovic, N. T., et al. 2020, *Nat. Astron.*, **4**, 1148
 Komacek, T. D., Showman, A. P., & Tan, X. 2017, *ApJ*, **835**, 198
 Komacek, T. D., Showman, A. P., & Parmentier, V. 2019, *ApJ*, **881**, 152
 Krenn, A. F., Lendl, M., Patel, J. A., et al. 2023, *A&A*, **672**, A24
 Lecavelier des Etangs, A., Deleuil, M., Vidal-Madjar, A., et al. 2003, *A&A*, **407**, 935
 Lendl, M., Csizmadia, S., Deline, A., et al. 2020, *A&A*, **643**, A94
 Lodders, K., Palme, H., & Gail, H. P. 2009, *Landolt Börnstein*, **4B**, 712
 Mai, C., & Line, M. R. 2019, *ApJ*, **883**, 144
 Mansfield, M., Line, M. R., Bean, J. L., et al. 2021, *Nat. Astron.*, **5**, 1224
 Maxted, P. F. L., & Gill, S. 2019, *A&A*, **622**, A33
 Maxted, P. F. L., Ehrenreich, D., Wilson, T. G., et al. 2022, *MNRAS*, **514**, 77
 Mazeh, T., Holczer, T., & Faigler, S. 2016, *A&A*, **589**, A75
 Newville, M., Otten, R., Nelson, A., et al. 2020, *Imfit/Imfit-py 1.0.1*, Zenodo
 Parmentier, V., & Crossfield, I. J. M. 2017, in *Handbook of Exoplanets*, eds. H. J. Deeg, & J. A. Belmonte (Cham: Springer International Publishing), 1
 Parmentier, V., Showman, A. P., & Lian, Y. 2013, *A&A*, **558**, A91
 Parmentier, V., Guillot, T., Fortney, J. J., & Marley, M. S. 2015, *A&A*, **574**, A35
 Parmentier, V., Fortney, J. J., Showman, A. P., Morley, C., & Marley, M. S. 2016, *ApJ*, **828**, 22
 Parmentier, V., Line, M. R., Bean, J. L., et al. 2018, *A&A*, **617**, A110
 Parmentier, V., Showman, A. P., & Fortney, J. J. 2021, *MNRAS*, **501**, 78
 Pavlenko, Y. V., Jenkins, J. S., Jones, H. R. A., Ivanyuk, O., & Pinfield, D. J. 2012, *MNRAS*, **422**, 542
 Piskorz, D., Buzard, C., Line, M. R., et al. 2018, *AJ*, **156**, 133
 Scandariato, G., Singh, V., Kitzmann, D., et al. 2022, *A&A*, **668**, A17
 Sheets, H. A., & Deming, D. 2017, *AJ*, **154**, 160
 Shporer, A., O'Rourke, J. G., Knutson, H. A., et al. 2014, *ApJ*, **788**, 92
 Soto, M. G., & Jenkins, J. S. 2018, *A&A*, **615**, A76
 Sudarsky, D., Burrows, A., & Pinto, P. 2000, *ApJ*, **538**, 885
 Vines, J. I., & Jenkins, J. S. 2022, *MNRAS*, **513**, 2719
 Vissapragada, S., Chontos, A., Greklek-McKeon, M., et al. 2022, *ApJ*, **941**, L31
 Wakeford, H. R., Visscher, C., Lewis, N. K., et al. 2017, *MNRAS*, **464**, 4247
 Wong, I., Kitzmann, D., Shporer, A., et al. 2021, *AJ*, **162**, 127

Appendix A: Raw CHEOPS light curves

The photometric time series delivered by the CHEOPS DRP (DEFAULT, $R=25$ pix) after removing outliers from the sigma clipping are shown in Figs. A.1 and A.2. A sample of 32 fitted detrending models (glint function) and the best eclipse model are represented by the green and brown curves, respectively. The files containing these light curves are available through the CHEOPS Mission Archive hosted by ESA.

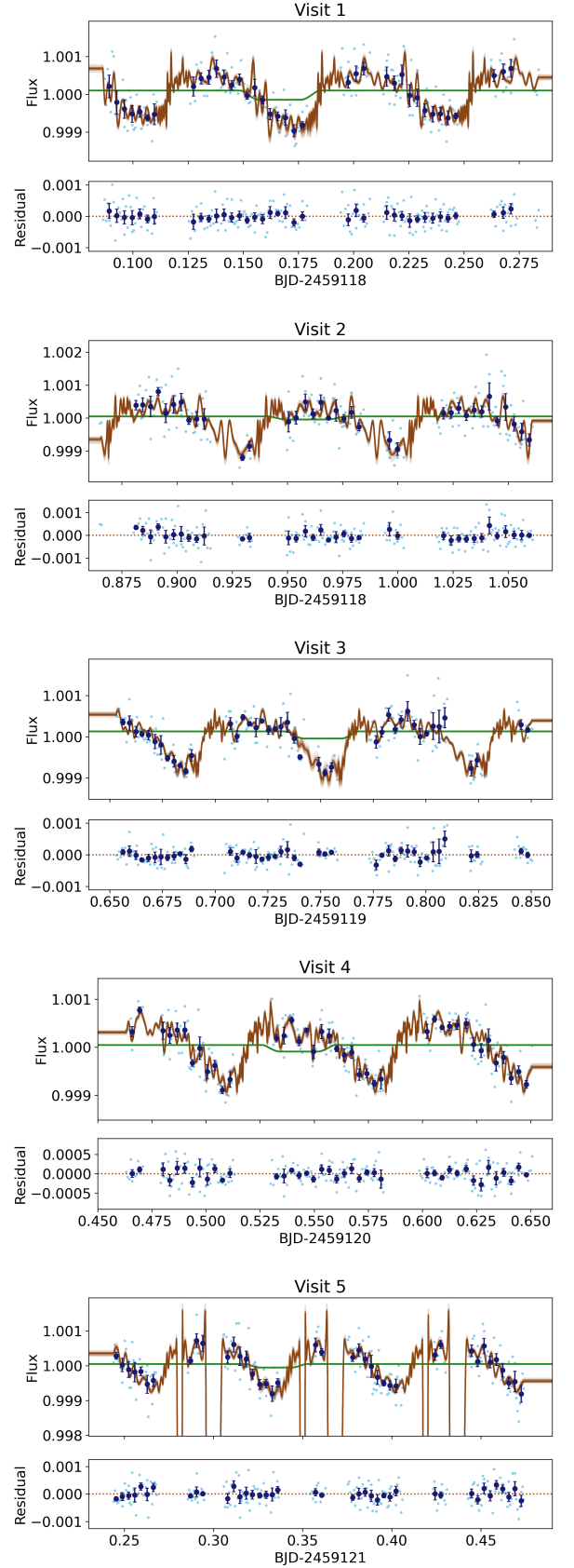


Fig. A.1. CHEOPS raw light curves of the eclipses of LTT 9779 b for visits 1, 2, 3, 4 and 5. The normalized photometric points (after sigma clipping) and the 5 min bins correspond to the light and dark blue symbols, respectively. The detrending (green curves) and best eclipse model (brown curve) are overplotted. The fit residuals are shown at the bottom panel of each light-curve panel.

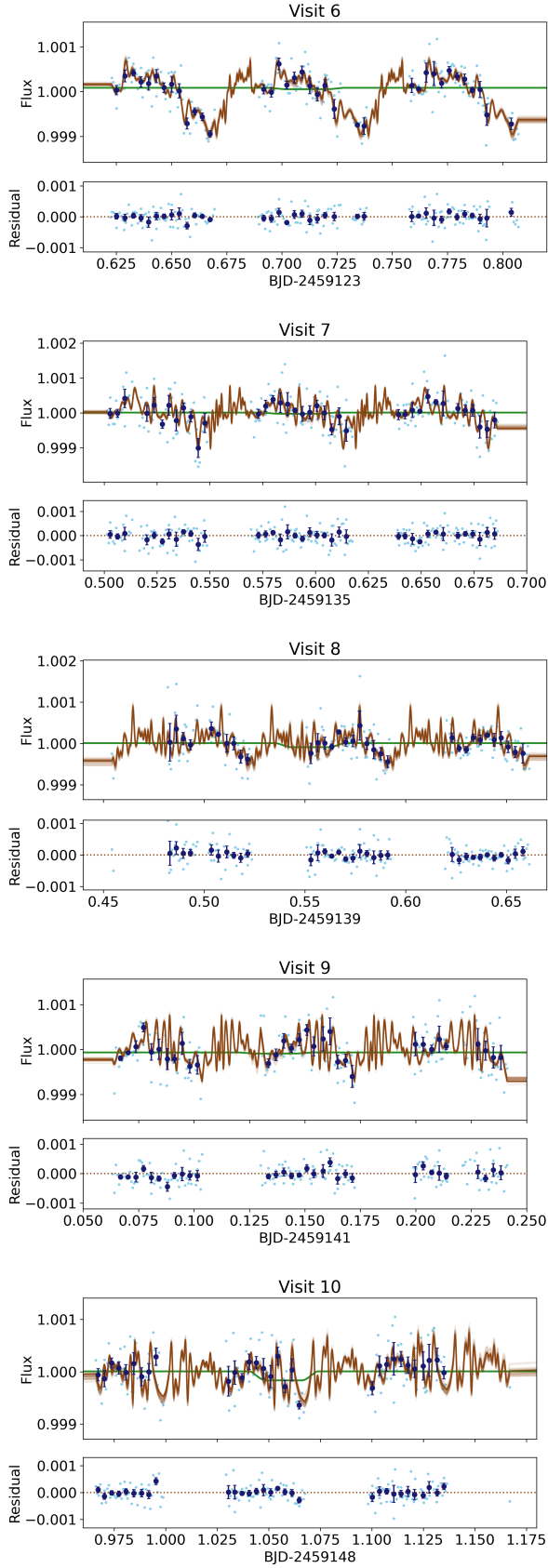


Fig. A.2. Same as Fig. A.1 for visits 6, 7, 8, 9 and 10.

Appendix B: Eclipse depths obtained with three different approaches

As described in Sect. 4.2, the CHEOPS light curves were analyzed with three different approaches: Two approaches used the PYCHEOPS package (differing in the filtering and detrending method), and one approach used an entirely independent analysis with different tools (see details in Scandariato et al. 2022). The resulting eclipse depths derived from each light curve by the three methods are fully compatible, as shown in Fig. B.1.

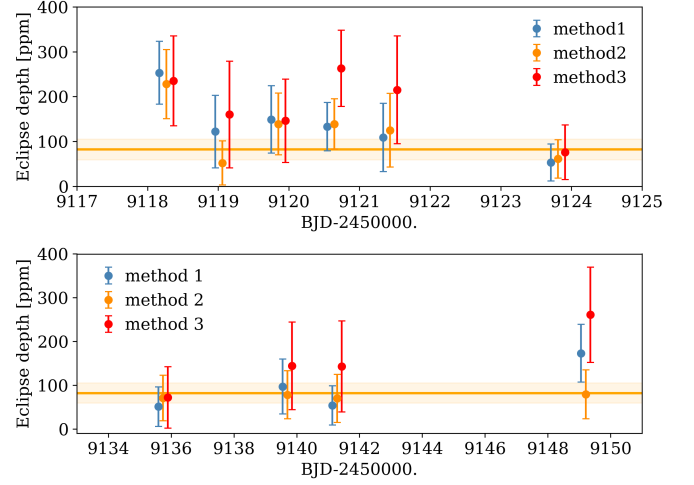


Fig. B.1. Results of the eclipse depths of individual fits performed with three different methods: Using PYCHEOPS, but with different filtering/detrending (methods 1 and 2), and using a fully independent approach (method 3). See the details in the text.

Appendix C: Corner plots

The posterior distributions of all the modeled parameters in the multivisit fit described in Sect. 4.3 have Gaussian-like shapes. No correlations were found between these fitted parameters. In Fig. C.1 we only show the distributions of the most relevant parameters for visualization purposes: The orbital period (P), the mean time of the transits (T₀), the eclipse depth (L), and the white-noise component in its log form (log σ_w).

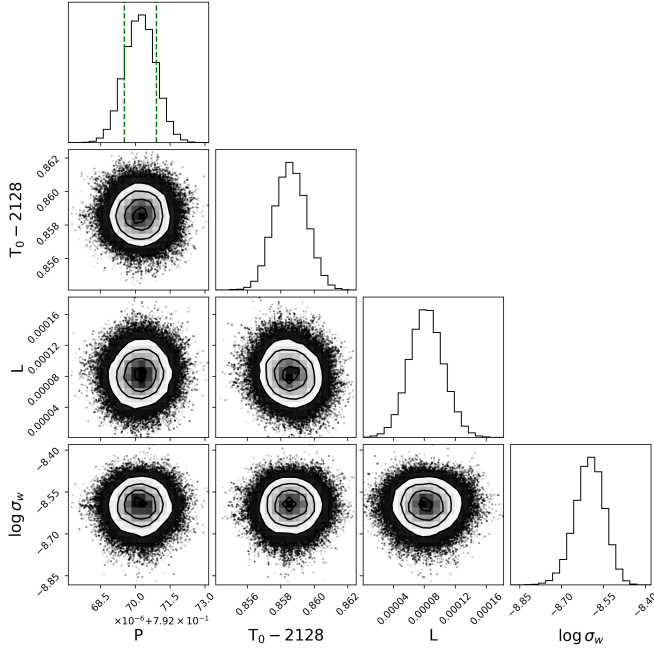


Fig. C.1. Corner plot of relevant parameters of the multivisit fit. The posterior distributions of all the modeled parameters have Gaussian-like shapes. For visualization purposes, we only show the distributions of the orbital period (P), the mean time of the transits (T₀), the eclipse depth (L), and the white-noise component in its log form (log σ_w).

Appendix D: Exploring the variability

As described in Sect. 4.3, in addition to the combined analysis of all the ten CHEOPS light curves, we also performed a separate analysis of the visits with a *large* and *small* eclipse detection. From these analyses, we obtained an eclipse depth that corresponds to $L=163\pm32$ ppm and 50 ± 32 ppm, respectively. The combined light curves and the best-fit model are presented in Fig. D.1. The distributions of the MCMC chains of the fitted eclipse depth (Fig. D.2) for the three cases analyzed in this work (all, only high, and only low values) show that we cannot statistically confirm the variability in the eclipses of LTT 9779 b with the data in hand, mainly because the individual detections have a low signal-to-noise ratio.

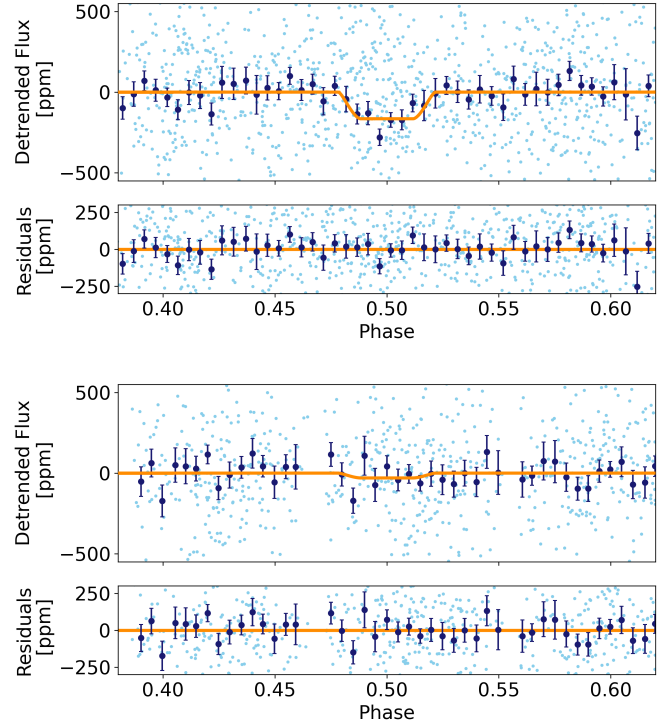


Fig. D.1. Phased CHEOPS light curves during the eclipses of LTT 9779 b. The combined phased light curve of the CHEOPS visits with deep (top) and shallow (bottom) estimates of the eclipse depths (as described in Sect. 4.3) are shown. The 7 min bins and the best-fit model are represented by the dark blue symbols and the yellow curve, respectively. The small panels show the respective residuals.

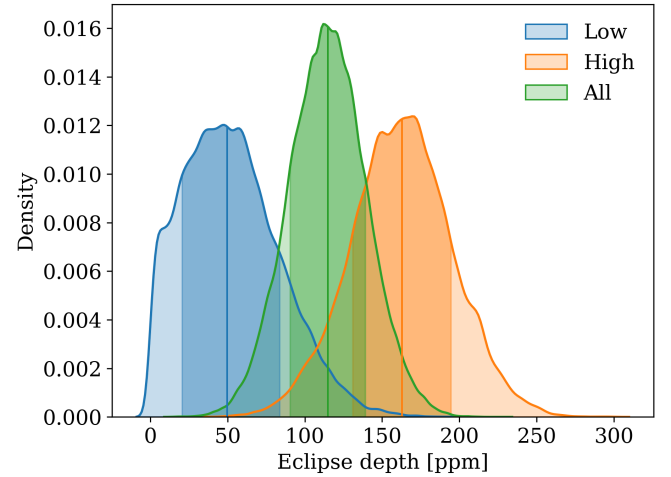


Fig. D.2. Density distributions of the MCMC walkers of the fitted eclipse depth. We show the distribution of the estimated depth using all the CHEOPS visits (green), and the visits with high (1, 2, 3, 4, 5, and 10; orange) and low (6, 7, 8, and 9; blue) depth estimates are shown. The vertical lines and shaded areas represent the median and the 1σ intervals.